ORBITING WIDE-ANGLE LIGHT COLLECTORS

by

Rasha Usama Abbasi

A dissertation submitted to the faculty of
The University of Utah
in partial fulfillment of the requirements for the degree of

Masters

Department of physics

The University of Utah

2003

THE UNIVERSITY OF UTAH GRADUATE SCHOOL

SUPERVISORY COMMITTEE APPROVAL

of a dissertation submitted by

Rasha Usama Abbasi

This dissertation has been read by each member of the following supervisory committee and by majority vote has been found to be satisfactory.

	Chair: Charlie C. H.Jui
	John N. Matthews
	Ben Bromley

THE UNIVERSITY OF UTAH GRADUATE SCHOOL

FINAL READING APPROVAL

To the Graduate Council of the University of Utah:

I have read the dissertation of Rasha Usama Abbasi in its final form and have found that (1) its format, citations, and bibliographic style are consistent and acceptable; (2) its illustrative materials including figures, tables, and charts are in place; and (3) the final manuscript is satisfactory to the Supervisory Committee and is ready for submission to The Graduate School.

Date

Charlie C. H.Jui
Chair, Supervisory Committee

Approved for the Major Department

Vally Vardeeny
Chair/Dean

Approved for the Graduate Council

David S. Chapman
Dean of The Graduate School

ABSTRACT

To be ..

To be

CONTENTS

LIST OF FIGURES

LIST OF TABLES

ACKNOWLEDGEMENTS

To be ..

Recognize faculty, friends, family but not the typist, editor or persons paid to produce the manuscript from draft copy. Recognize funding, special permission to reproduce figures and copyrighted material.

CHAPTER 1

INTRODUCTION

1.1 Motivation

Discovering cosmic rays with energies beyond the GZK cut off (around 6×10^{19} eV) [8] [9] made us realize that there are many remaining questions . Mainly; where do these rays come from , how do they propagate through the cosmic microwave background in the interstellar and intergalactic space to reach the earth and is special relativity preserved at ultra high energies . To find the answers, we are obligated to determine some information about these particles that we are detecting, mainly there energies, chemical composition and arriving direction .

1.2 Anisotropy

Studying the arrival direction of cosmic rays arrive is essential to understanding the sources of the ultra high energy cosmic rays. Cosmic ray particle trajectories get bent by the regular galactic magnetic field and this produces a diffusive motion in the galaxy. This deflection is described by Lamour radius:

$$R_l = \frac{E}{300 * (Hz)} \tag{1.1}$$

where R_l is Lamour Radius measured in cm, E is the energy of the particle in eV, H is the Magnetic Field in gauss, z is the charge of the particle .

Thus a particle passing through a magnetic cloud with length L will experience an angular deflection = L/R_l radians.

As the energy of the particle increases ,the deflection decreases. At ultra high energies, the deflection to the particles path becomes small enough for it's arrival direction to give meaningful information about the origin.

If galactic sources are mainly in the galactic plane, anisotropy for a cosmic ray particle will develop towards the galactic disk. But, if sources are extra-galactic and centered on the local super cluster of galaxies, we expect anisotropy to be directed at higher galactic latitude.

Anisotropy measurements are subject to many problems. These include is the statistically limited data at ultra high energies and the non-uniformality acceptance of cosmic rays direction .

1.3 Composition

.

The composition study also provides clues as to the source of these particles. However, in order to determine what these particles are, we must look at the distribution of the first interaction point of the particle in air. One can determine it's type by comparing it to predicted models for different particles. Knowing that the light in the beginning of the interaction is low, looking for such a distribution was avoided and the study of the depth of the shower maximum, X_{max}, was adapted.

Showers that are generated by iron nuclei will hit air, and on average, have a shallower X_{max} than a one generated by a proton nuclei. However, due to the significant fluctuation in the X_{max} distribution; an event by event discrimination is not possible and we are obligated to perform a statistical study of the average of X_{max} .

A Fly's Eye composition study [7] reported that the composition of the cosmic rays change from heavier nuclei (iron) below 10^{18}eV to a lighter one (proton) above 10^{18} eV.

Since OWL observing aperture will be orders of magnitude greater than the current High Resolution Fly's Eye detector, more data will be collected at Ultra High Energy, UHE, and the composition will be studied with better confidence and higher limits of energy.

1.4 The Spectrum

.

The observed flux of cosmic rays appears to obey a differential power law spectrum:

$$\frac{\mathrm{d}N}{\mathrm{d}E} = E^{-\alpha} \tag{1.2}$$

where α is the spectral index. The flux varies from 1 particle per cm^2 per steradian per hour at 10^{12} eV to 1 particle per km^2 per steradian per year at 10^{20} eV. The spectral index is virtually unchanged over a very large energy range. However, there are some small features at "the knee", $\sim 10^{15}$ eV ,the spectral index steepen from 2.7 to 3.0. Below 10^{18} eV the index increases to 3.27 and finally just above 3×10^{18} eV "The ankle" the spectral index relaxes again to 2.7.

It has been proposed [2] that the change of the index at the knee is due to free diffusion of cosmic rays through the galactic disk, as the energy of particles increases, the Lamour radius increases and particles with smaller charge to mass ratio such as protons begin to escape. But iron diffuses when it gets to an energy around 3 Eev. Beyond that energy, cosmic rays energies are proposed to come from a few mega parsecs away extra galactic sources, with a much flatter injection spectrum than that of a galactic source.

1.5 Studying Cosmic Rays

.

Cosmic ray detection beyond 10^{14} eV is indirect due to the severe drop in the flux being produced as mentioned above. One technique frequently chosen is to take an advantage of the fact that interactions between cosmic ray particles and the atmosphere produces a correlated cascade of secondary particles, this cascade is called the extensive air shower, EAS.

The EAS starts primary with pi-mesons particles, the charged ones will live long to interact with other nucleus in the atmosphere followed by subsequent collisions that are similar to the primary one, this is so called the "hadronic shower". However neutral pion will most probably decay to a pair of γ-rays, γ-rays will interact with nucleus in air producing (e^-, e^+), and each will produce 2γ rays via "bressmtrahlung" process. This cascade is called the "electromagnetic shower".

EAS can be observed by detecting the fluorescence light that is primarily being produced by electrons. To study this light we need to determine some shower parameters as the longitudinal profile, and the lateral distribution.

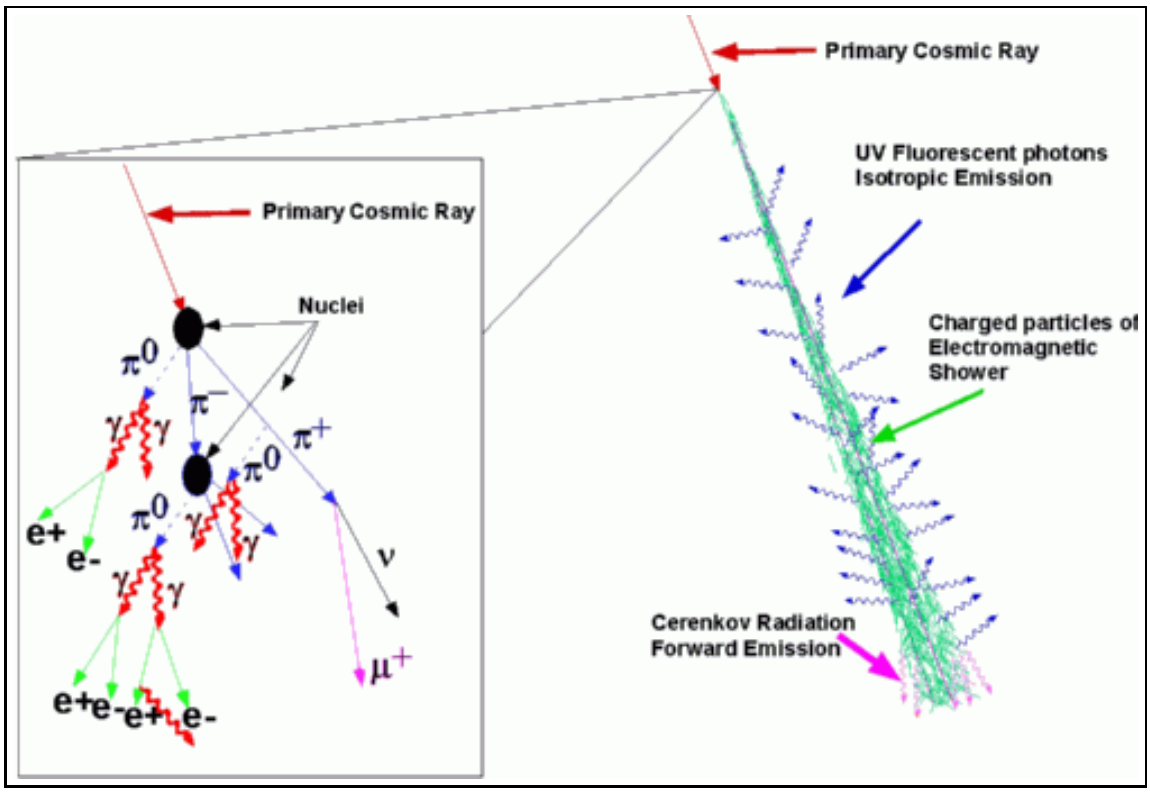

Figure 1.1. Extensive Air Shower

1.6 Longitudinal Shower Development

.

The shower multiplicative process starts with a photon that holds an energy equals to E_o, that produces (e^-, e^+) with an energy equal to $E_o/2$ each, and each will produce 4γ rays with energy equal to $E_o/4$. This process will continue tell the energy is equal to E_c " The critical energy" , where E_c is the energy at which the dominant loss is by ionization rather by bremsstrahlung and it's equal to 82 Mev .At this point the shower reaches it's maximum development.

N_{max} = (1.1 to 1.6) E_c (Gev) .

where N_{max} is the number of particles at the shower maximum .

The number of electrons at each point of the shower can be represented as a function of the slant depth by Gaisser Hillas function [11].

$$N_e(X) = N_{max} * (\frac{X - X_o}{X_{max} + X_o})^{(X_{max} - X_o)/\lambda} * exp(\frac{X_{max} - X}{\lambda}) \tag{1.3}$$

where X_o is the point of the first interaction and its equal to 37.1 gm/cm^2 , and λ is a constant equal to 70 gm/cm^2 .

1.7 Lateral Distribution

the electron lateral distribution (density) is [10].

$$\rho(r) = \frac{N}{r^2} f(s, \frac{r}{r_m}) \tag{1.4}$$

where N is the total number of electrons, s is the shower effective age parameter, r_m is Moliere radius for multiple scattering, and f is Nishimura Kamata function.

where

$$s = \frac{3x}{x + 2x_{max}} \tag{1.5}$$

and

$$f\left(s, \frac{r}{r_m}\right) = \left(\frac{r}{r_m}\right)^{(s-2)} \left(1 + \frac{r}{r_m}\right)^{(s-4.5)} \left(\frac{\Gamma(4.5 - s)}{2\pi\Gamma(s)\Gamma(4.5 - 2s)}\right) \tag{1.6}$$

CHAPTER 2

SHOWER MONTE CARLO

This chapter contains the describtion of the atmospheric and shower simulation of OWL. It describes the shower geometry and profile generation and the light propagation through the atomsphere i.e. scatterings and the absorptions. Note that this model is adapted from the HiRes simulation with modifications due to the new conditions.

2.1 The Atmosphere

The atmospheric simulation can be described by four components:

1. Raleigh scattering.
2. Ground aerosols scattering.
3. Ozone absorption.
4. Cloud scattering.

Genrally light scattering is described by two parameters, first is the light cross section, second is the phase function $P = P(cos(\theta_s))$ where θ_s is the scattering angle.

2.1.1 Raleigh Scattering

Raleigh scatteing parameter are

- the cross section β_R which is given by:

$$\beta_R = 100 \cdot \frac{\rho(h)}{x_R} \cdot \left(\frac{400}{\lambda}\right)^4 \tag{2.1}$$

  where $\rho(h)$ is the air density in gm/cm^2, h is the altitude in m, andx_R is the mean free path = 2970 gm/cm^2 at wavelength $\lambda = 400$ nm.

- the phase function which is given by:

$$P(cos(\theta)) = (\frac{3}{16}\Pi)(1 + cos^2\theta) \tag{2.2}$$

2.1.2 Aerosols Scattering

Aerosols scattering paramer is given by:

$$\beta_a(\lambda) = \frac{\rho_a}{L_a(\lambda)} \tag{2.3}$$

where L_a is the scattering length at the ground and ρ_a is the aerosols reduced density.

2.1.3 Ozon Absorption

the ozone absorption extinction length (m) is

$$\frac{1}{L_{o3}} = 9.87 \times 10^{-7} \cdot \alpha_o 3(\lambda) \cdot \rho_{o3}(\lambda) \tag{2.4}$$

where $\alpha_o 3$ is the absorption dependent coefficient and ρ_{o3} is the altitude dependent concentration.

2.1.4 Cloud Scattering

The clouds are simulated with a uniform density. The scattering length β_{clo} inside the clouds is,

$$\beta_{clo} = \frac{\tau}{(h_{top} - h_{base})} \tag{2.5}$$

where τ is the optical depth, h_{base} is the cloud base hegiht, and h_{top} in the cloud top height.

2.2 Shower Simulation

The shower is charechtarized by three parameters:

1. The track geometry generation.
2. The energy of the primary particle.
3. The profile generation.

2.2.1 Track Geometry Generaiton

The track geometry is generated in two steps.

- The shower core which could lie outside the field of view of the detector since the detector would observe part of it .
- The track trajectory which is defined by (θ, ϕ) and it is generated isotropically in all directions.

2.2.2 Energy Generation

The energy is generated with a fixed value.

2.2.3 Profile Generation

The profile of the shower followes Gaisser-Hillas function [11]

$$N_e(X) = N_{max} * (\frac{X - X_o}{X_{max} + X_o})^{(X_{max} - X_o)/\lambda} * exp(\frac{X_{max} - X}{\lambda}) \qquad (2.6)$$

where X_o is generated with an exponential random function (with a mean =35 gm/cm^2), X_{max} is generated by a gaussian distribution (with a mean = $< X_{max} > + ER * (Log_{10}(Energy) - 18.0)$ where $< X_{max} >$ =725 gm/cm^2 at energy = $10^8 eV$, and ER is the elongation rate = 55 gm/cm^2),λ is constant = 70 gm/cm^2,and N_{max} is chosen such that the integral of the profile plus the Energy lost will provide us with the origional energy of the primary particle [3].

$$E_{tot} = E_{corr} + 2.18 \cdot \int N_e(X) \mathrm{d}X$$

where E_{tot} is the energy of the primary particle, and E_{corr} is the energy loss.

CHAPTER 3

EVENT RECONSTRUCTION DATA SELECTION

3.1 Motivation

After shower generation has been completed, we are able to proceed with the event reconstruction, including determination of shower geometry and finally energy. This process is divided into:

1. plane reconstruction
2. track reconstruction
3. profile reconstruction.

After applying reconstruction to the generated events, a study of selection cuts is made to select those cuts which will optimize energy and angular resolution while retaining reasonable detector acceptance. This study will provide us with the true aperture of the detector and subsequently characterize the ability of the detector to "do physics".

3.2 Reconstruction

3.2.1 Plane Reconstruction (rcpln)

The first step in the data reconstruction procedure is to determine the shower detector (SD) plane. The SD plane can be formed from the direction of the triggered pixels, where we take the the plane to contain the detector "as a point" and the shower track as a line. The plane normal vector is determined by a χ^2 fit:

$$\chi^2 = \sum_{i=1}^{N} \frac{(\hat{n} \cdot \hat{n_i})^2 \, S_i}{\sigma_i^2} \tag{3.1}$$

where $\hat{n}$ is the unit vector normal to the plane, $\hat{n_i}$ is the unit vector in the direction of the i^{th} hit pixel, S_i is the number of photoelectrons triggering the i^{th} pixel, and σ_i is the angular uncertainity for the pixel which we take to be about 0.07°.

3.2.2 Track Reconstruction (rctrk)

The second step in the reconstruction is to calculate the track trajectory. Since OWL has two orbiting detectors, the track is simply determined by intersecting the SD planes ($\hat{n}_{SD1} \times \hat{n}_{SD2}$) found for the two detectors [16].

3.2.3 Profile Reconstruction (rcpfl)

After the shower geometry is obtained, we calculate the shower profile. Gaisser-Hillas [11] profile is fit to the observed pixel signals:

$$\chi^2_{pfl} = \sum_{i=1}^{N} \frac{(\phi_i^m - \phi_i^p)^2}{\sigma_i^2}. \tag{3.2}$$

where ϕ_i^m is the number of photoelectrons reconstructed for each tube, ϕ_i^p is the number of photoelectrons generated by MC simulation, and σ_i^2 is the uncertainity calculated after adding the Poisson fluctuation, the sky noise, and the statistical uncertainity.

3.3 Quality Cuts

Poorly reconstructed events are rejected by applying quality cuts to the reconstructed data. These cuts are optimized to get the best energy and angular resolution while retaining reconstructible aperture, we describe these in the following section.

3.3.1 $\chi^2/ndof$:

The value of χ^2_{pfl}/ndof of less than 12 in the profile fit. Those with larger values represent unacceptably poor fits.

3.3.2 zenith angle:

The Zenith angle of the shower is generated from 90° to 180°. Angles that are less than 93° are rejected because the SD planes would be flat. Accordingly the

reconstruct such events will be degraded.

3.3.3 Opening angle:

The opening angle is the angle between the reconstructed SD planes. Events with openning angles that are less than 10° are rejected because the two planes are too close to each other for the reconstructed geometry to be reliable.

3.3.4 Track length:

This cut rejects events with a track length shorter than 0.7°, (notice here that the pixel size is 0.07°). Short tracks will not contain enough information about the geometry of the track, such events are not dependable. See figure 3.1.

3.3.5 Photo Electron Per Good Tube:

The average number of photoelectrons per good tube should be larger than 5.2. This cut will eliminate events that are caused by low energy events and noise sources.

3.4 Conclusion

The following figures describe the energy resolution as shown in figures 3.2 and 3.3, in addition to the angular resolution as in figures 3.4 and 3.5 for the energies 3×10^{19}, 5×10^{19}, 7×10^{19}, 9×10^{19}, 1×10^{20} and 3×10^{20} consequently, after applying reconstruction and quality cuts to the generated events.

The main reason for the energy resolution study is to know the ability of the detector to do physics for a certain energy range. We notice the energy resolution is better for higher energies than those of lower energies. In other words for higher energies we have smaller offsets and smaller RMSs. The angular resolution plots also have a better quality resolutions for higher event energies. This is a direct result of the fact that events with higher resolution will interact at higher points in the atmosphere than those of lower energies and we would be able to see a larger fraction of the shower.

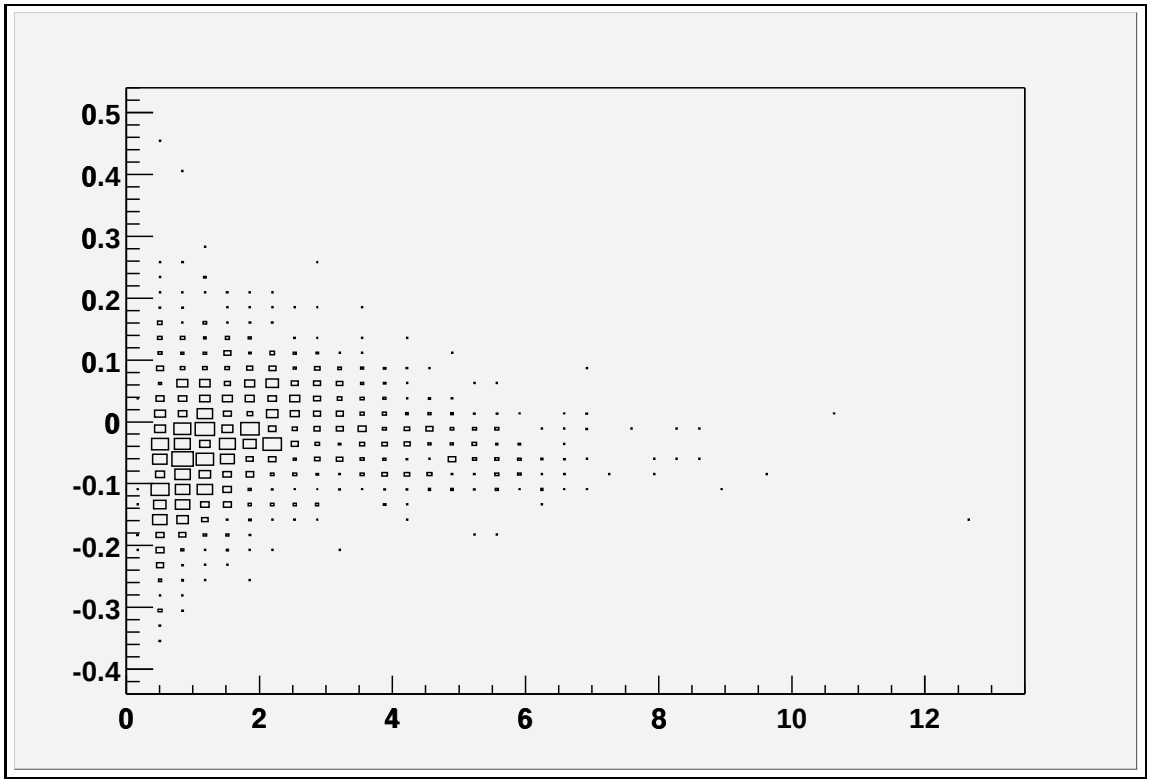

Figure 3.1. From top to bottom energy resolution vs. track length for a simulated shower with an energy of 9×10^{19} eV, note that events that are less than 0.7° are rejected becasue of there poor quality

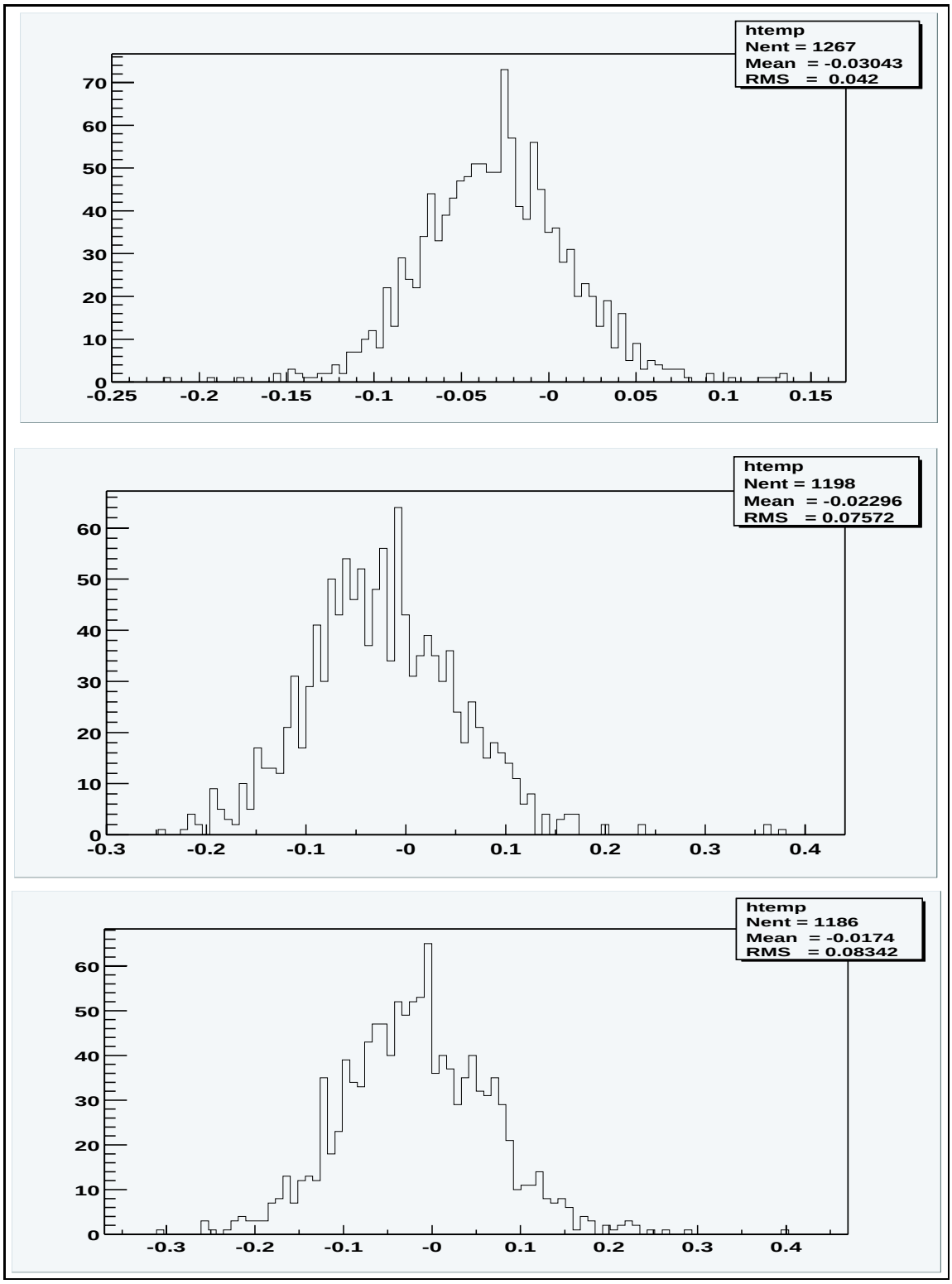

Figure 3.2. From top to bottom energy resolution for the energies 3×10^{20}, 1×10^{20}, 9×10^{19} eV after applying the quality cuts on the reconstructed data, note that the RMS is smaller for the larger energies

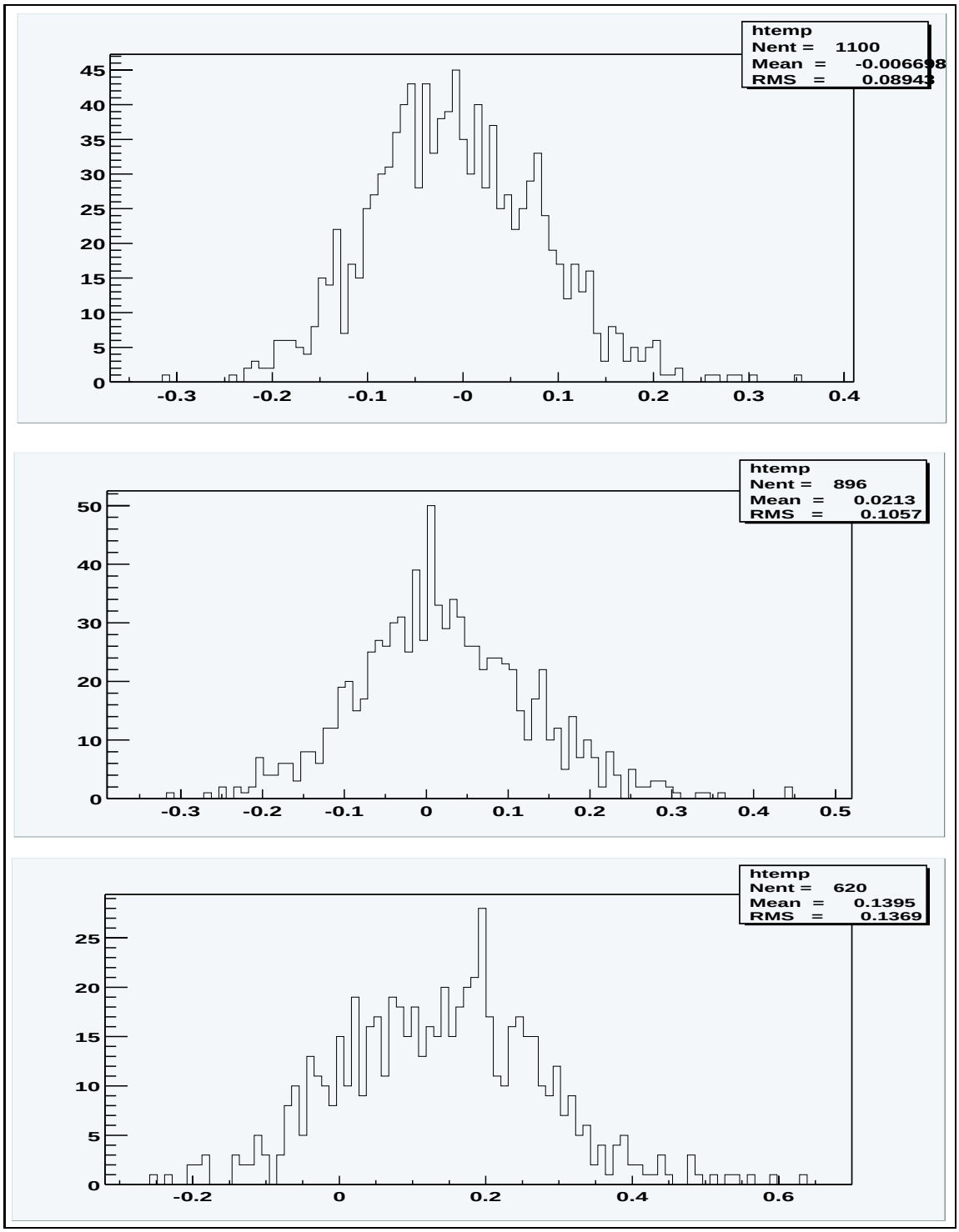

Figure 3.3. From top to bottom energy resolution for the energies 7×10^{19}, 5×10^{19}, 3×10^{19} eV after applying the quality cuts on the reconstructed data, note that the RMS is smaller for the larger energies

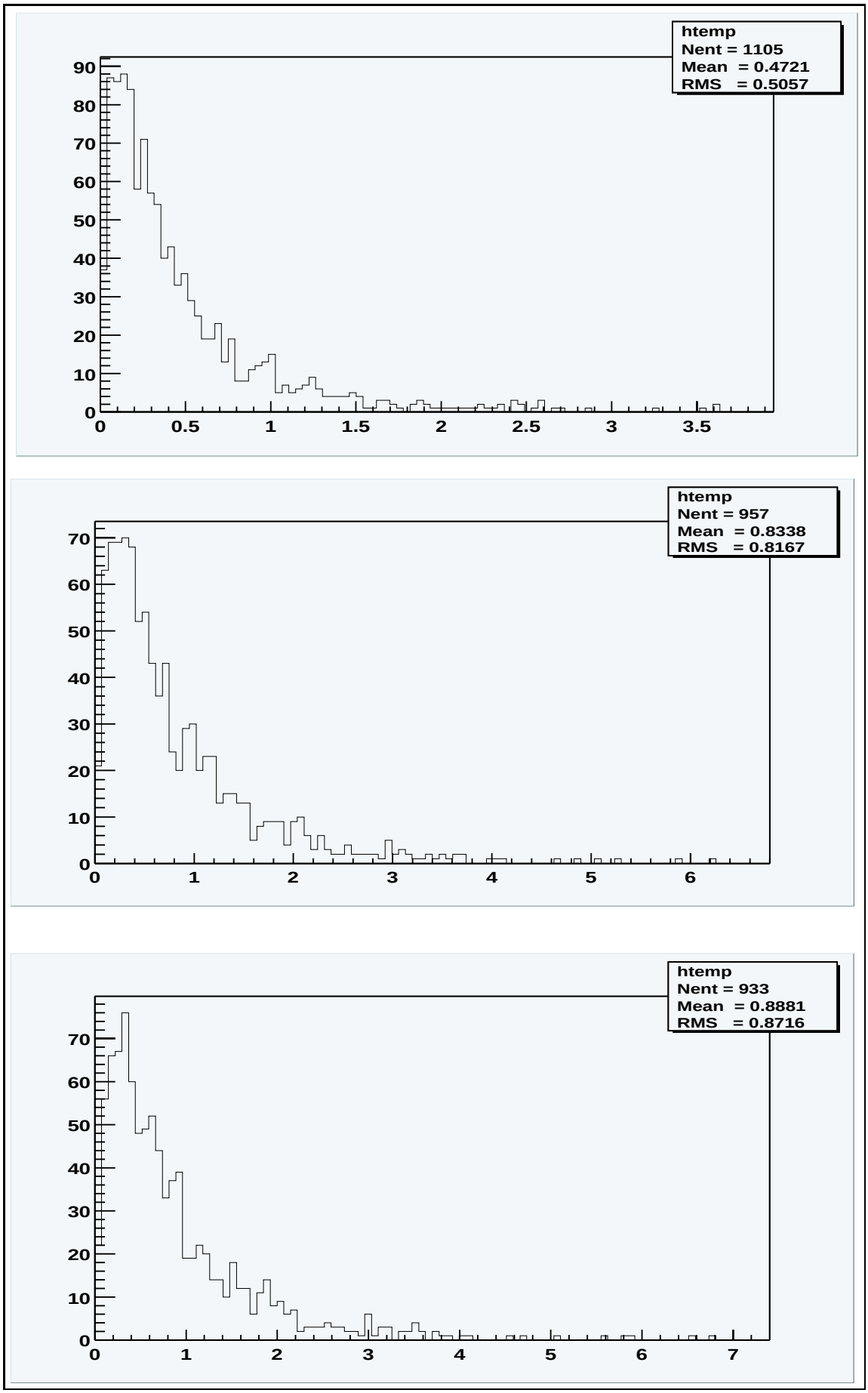

Figure 3.4. From top to bottom angular resolution for the energies 3×10^{20}, 1×10^{20}, 9×10^{19} eV after applying the quality cuts on the reconstructed data, note that the RMS is smaller for the larger energies

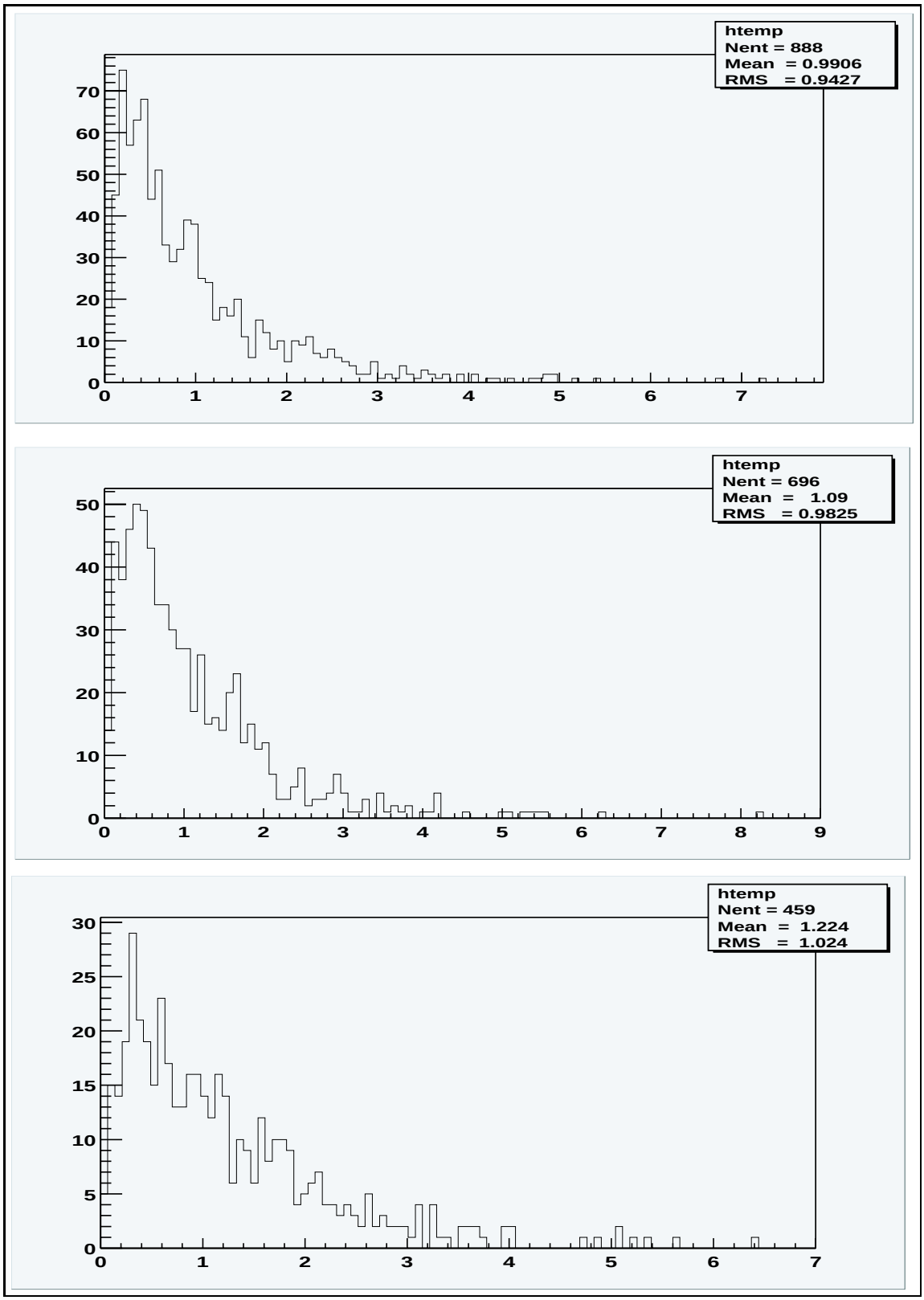

Figure 3.5. From top to bottom angular resolution for the energies 7×10^{19}, 5×10^{19}, 3×10^{19} eV after applying the quality cuts on the reconstructed data, note that the RMS is smaller for the larger energies

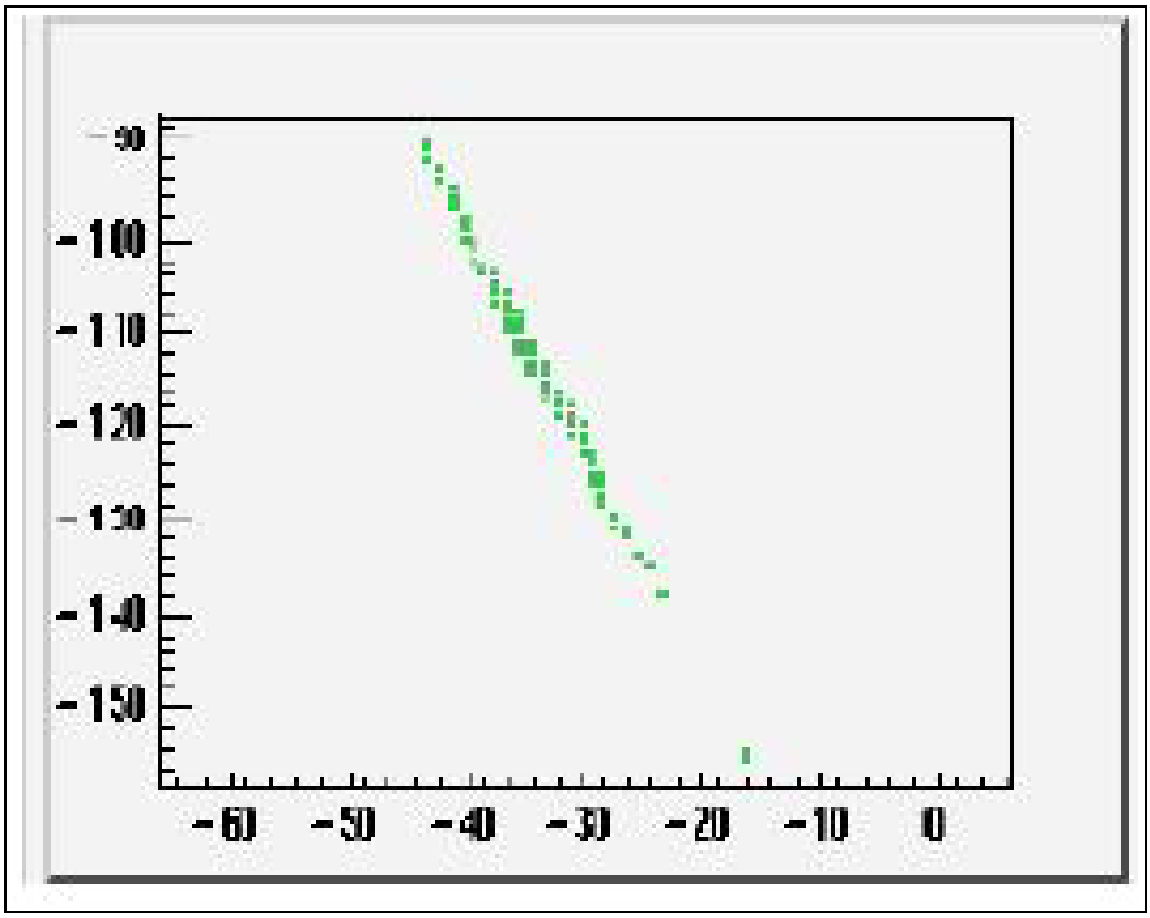

Figure 3.6. The vertical angular position vs. the horizontal angular position for an event generated by OWL as seen by 1^{st} eye of the detector. Note that the larger the box is the more light it detected.

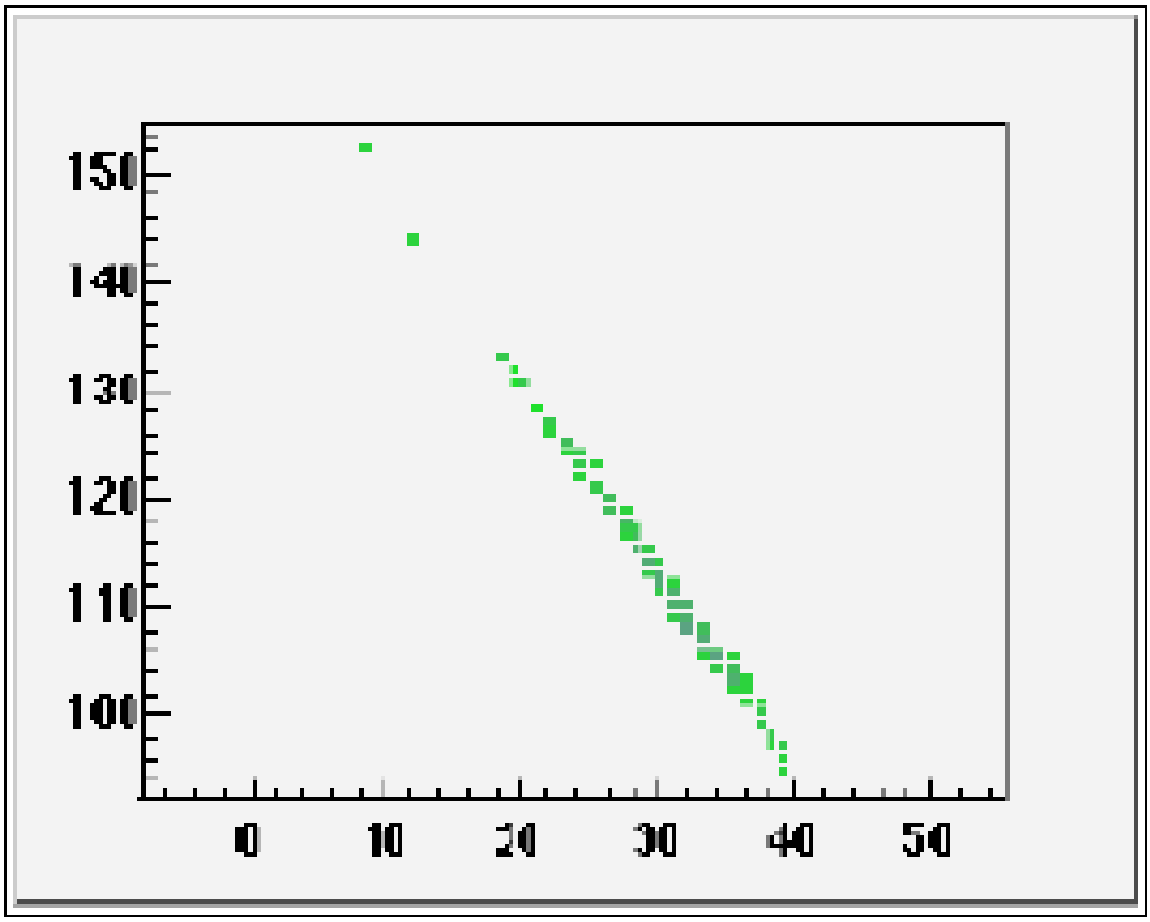

Figure 3.7. The vertical angular position vs. the horizontal angular position for an event generated by OWL as seen by 1^{st} eye of the detector. Note that the larger the box is the more light it detected.

CHAPTER 4

APERTURE CALCULATION

4.1 Aperture

The statistical power of a cosmic ray detector is quantified by its aperture, which is the convolution between solid angle and detection area. From the point of view of experimental design, the aperture determines the rate at which events are detected for a given model of cosmic ray flux. Conversely, once an experiment in online, the aperture is needed to convert observed event count and exposure time to differential flux. The differential flux is the number of particles collected by the detector per unit time per unit area per unit energy $[m^2\ sr^{-1}\ s^{-1}\ eV^{-1}]$.

In practice, the differential flux is determined from the number of events observed in time T, within an energy bin spanning the interval (E=dE/2, E+dE/2), using the formula:

$$j(E) \approx \frac{\Delta N}{\Delta E\ T\ A\Omega(E)} \tag{4.1}$$

where E is the bin center and dE is the full width of the energy bin.

In order to calculate the aperture that is covered by the detector we start with the generation aperture of the detector.

$$A\Omega_{gen} = \pi^2\ R^2 \tag{4.2}$$

where R is equal to 500 km.

Follows that A $\Omega_{gen} = 2.467 \times 10^6 \quad km^2$ sr.

As a result the triggered aperture is which is done by simulating artificial events fig (4.1) and it's calculated as follows.

$$A\Omega_{trig} = A\Omega_{gen} \frac{\sharp triggered\ events}{\sharp generated\ events}. \tag{4.3}$$

The same method applies for the reconstructed aperture see fig (4.2).

$$A\Omega_{rec} = A\Omega_{trig}\frac{\sharp reconstructed\, events}{\sharp\, triggered events}. \tag{4.4}$$

The number of reconstructed events is calculated after passing the generated events through reconstructing programs that were mentioned in the previous chapter (rcpln, rctrk and rcpfl). Afterwards quality cuts are applied to the data.

The uncertainty in the generated aperture and the reconstructed aperture is calculated by the following equation according to binomial statistics [4].

$$\sigma^2 = N \cdot p \cdot (1 - p). \tag{4.5}$$

where N is the total number of generated events, p is the probability for the events to get triggered. A fit is applied to the reconstructed aperture to get the average value at which the aperture becomes constant and it is $0.845\times\ 10^6\ km^2sr$.

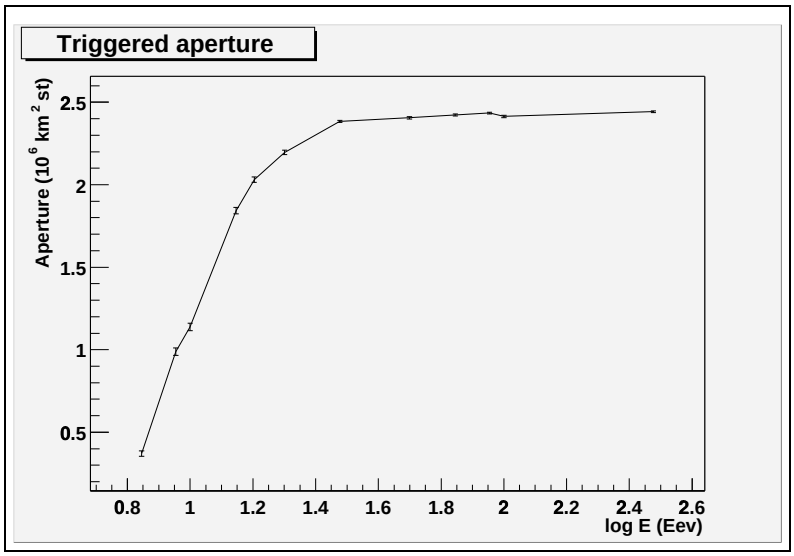

Figure 4.1. The trigger aperture

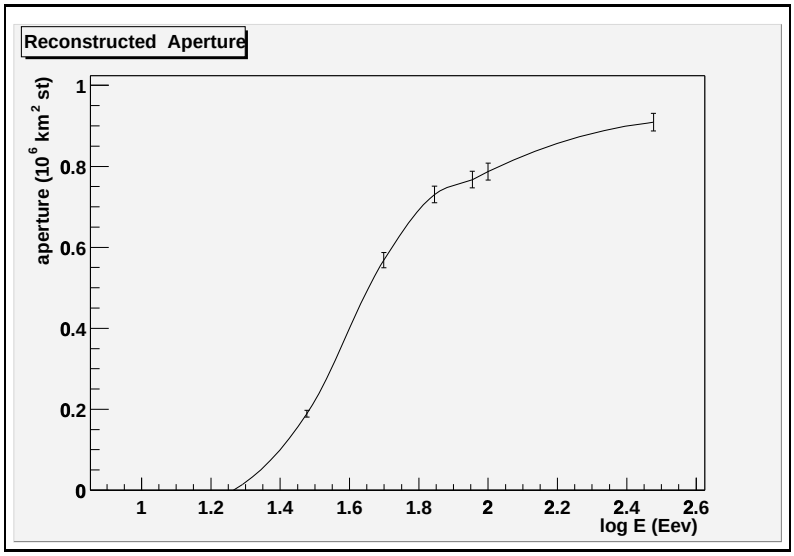

Figure 4.2. The reconstruction aperture

Table 4.1. Number of Monte Carlo events at stages of reconstruction the columns are : energy, number of events generated at this energy, number of triggered events, number of events passing the profile reconstruction, and finally the number of events that passing quality cuts.

E(eV)	♯ Gen	♯ Trig	♯ Rcpfl	♯ Cuts
3.0×10^{20}	3000	2970	2195	1105
1.0×10^{20}	3000	2935	1845	957
9.0×10^{19}	3000	2960	1827	933
7.0×10^{19}	3000	2946	1627	888
5.0×10^{19}	3000	2925	1241	691
3.0×10^{19}	6000	5796	903	459
2.0×10^{19}	3000	2670	44	0
1.6×10^{19}	3000	2469	2	0
1.4×10^{19}	3000	2240	0	0
1.0×10^{19}	3000	1383	0	0
9.0×10^{18}	3000	1201	0	0
7.0×10^{18}	3000	450	0	0

Table 4.2. Number of events per year per energy bin .

$log_{10}(E(eV))$	♯ events	$log_{10}(E(eV))$	♯ events
1.7	804.73	2.6	23.75
1.8	544.06	2.7	16.06
1.9	367.83	2.8	10.86
2.0	248.68	2.9	7.34
2.1	168.13	3.0	4.96
2.2	113.67	3.1	3.35
2.3	76.85	3.2	2.27
2.4	51.96	3.3	1.53
2.5	35.13	3.4	1.03

4.2 Event Rate Calculation

On a more partial level, we need to calculate is the rate of events collected by the detector per energy bin. But since we don't have real data from the detector we will use Fly's Eye stereo experiment flux results [7], shown in figure (4.3) to calculate the total number of particles expected to be seen in a year.

Figure (4.3) shows a plot of $J(E) \cdot E^3$ vs Log(E).

$$Log(JE^3(eV)) = 24.09 + 0.30 \cdot Log\left(\frac{E}{10^{18}}\right). \tag{4.6}$$

And we get:

$$j(E) = (4.9{\cdot}10^{18}) \cdot E^{-2.7}. \tag{4.7}$$

$$N = T \cdot \int_{E_i - \Delta E/2}^{E_f + \Delta E/2} A\Omega(E) \cdot j(E)\, \mathrm{d}E. \tag{4.8}$$

The number of events collected by the detector in a year duration of time (T) that hold energies between E_i (5×10^{19}) and E_f (3×10^{20}) equal to 2375.79 event, Table (4.2) shows the number of events per energy bin in the logarithmic scale where each bin is 0.1 interval.

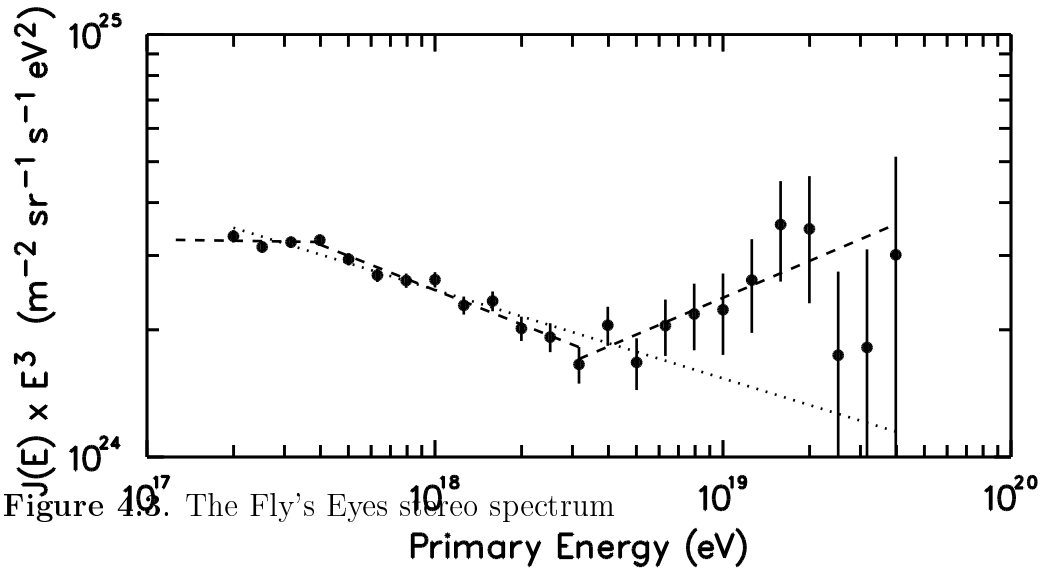

Figure 4.3. The Fly's Eyes stereo spectrum

CHAPTER 5

OWL OPTICS

5.1 OWL OPTICAL SYSTEM OVERVIEW

The proposed OWL detector is composed of two satellites at 1000 km height and 500 km separation. They view a common volume of the sky and are tilted near the nadir point. The choice of the detector orbit is based on the requirement to obtain a large field of view (FOV) and in consequence a large collection aperture. One challenging aspect of such a design is the need to keep a simple compact configuration.

OWL optical system contains figure (5.1).

- wide-angle viewing camera (40° FOV).
- 3.0 meter diameter aspherical front surface with a planer back surface corrector plate.
- spherical focal plane surface (2.3 m diameter, 3.0 m radius of curvature, and 3.15 m focal length).
- spherical mirror (7.1 m diameter, 6.0 m radius of curvature).

5.2 Spherical Aberration

For a sufficiently small aperture, light entering will be confined near the optical axis and are " par-axial". These will be focused at equal distances from the mirror surface at the focal length resulting in a spherical focal surface. However the large aperture required for the OWL mission means that light will enter in large bundles, Rays which come further away relative to the optical axis will be reflected

at a shorter distance resulting in the formation of an extended spot (spherical aberration).

To solve such a problem Schmidt designed a corrector plate that is placed at the entrance aperture. Its function is to bring all rays coming from the same angle to the same point on the focal surface. With this set up we will be able to accumulate a large field of view with an exact compensation to the spherical aberration produced by the spherical mirror.

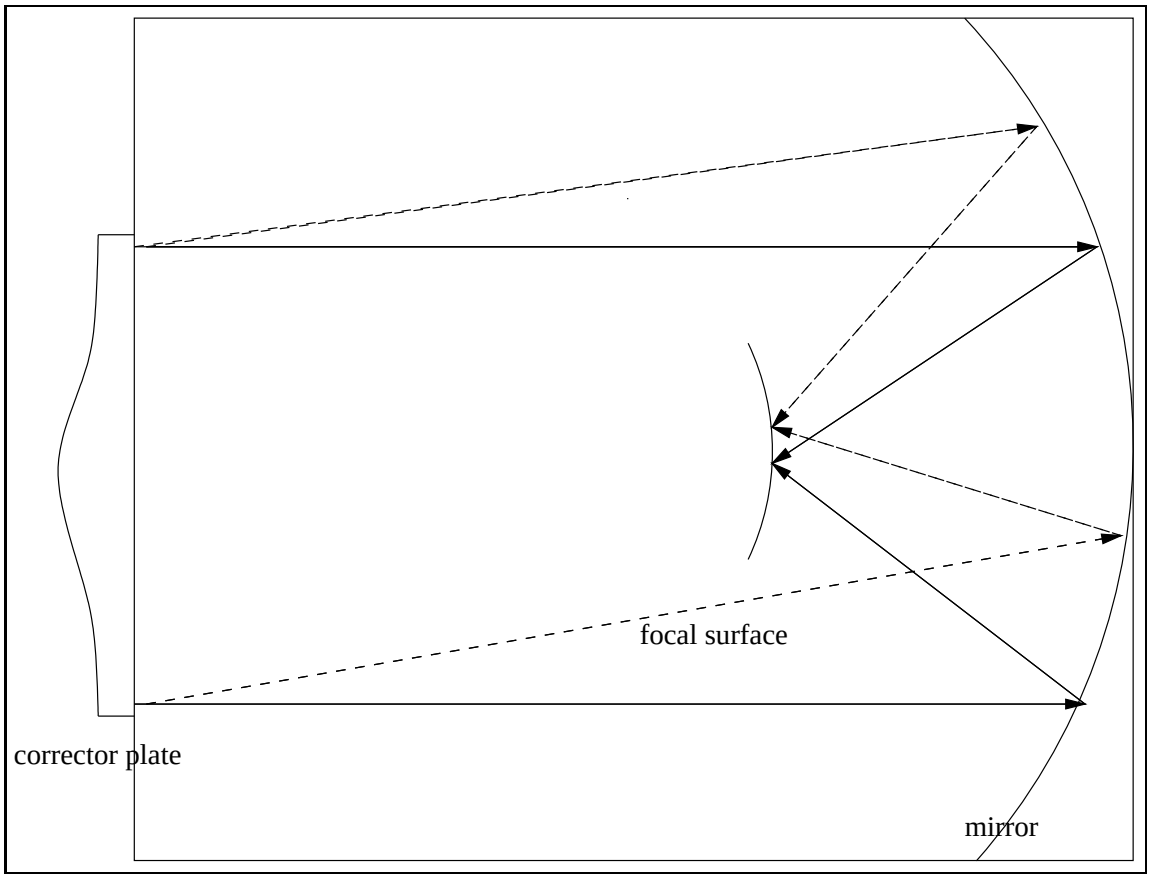

Figure 5.1. Schmidt camera geometry

5.3 Schmidt Lens

The profile of the corrector plate is given as discussed in [1].

$$T(r) - T(0) = \frac{(r^4 - Ar^2)}{32(n2-1)f^3} \tag{5.1}$$

where

$$A = \frac{3}{2}R_d^2. \tag{5.2}$$

where T(r) is the thickness of the corrector plate at a radial distance r from the center, f is the focal length of the mirror, n2 is the refractive index of the plate 1.5, and R_d is the radius of the entrance from the center of entrance.

5.4 Simulation Description

The following is a description of two versions of the Schmidt telescope, the first is a simple arrangement without the corrector plate and the second has a Schmidt corrector plate implemented in it. The ray tracing goal is to study the contribution of the corrector plate in enhancing the image quality.

5.5 Mirror Optics

The program simulate the incident light that passes through a point (x,y,z) and parallel to the unit vector $\hat{n} = a\hat{i} + b\hat{j} + c\hat{k}$.

The light than get reflected by the primary mirror.

To trace the reflection we follow these steps below :

1. First, we Calculate the point at which the incident beam hits the mirror (x_1, y_1, z_1).

   Since the line equation is.

$$x_1 = x + a \cdot t \tag{5.3}$$

$$y_1 = y + b \cdot t \tag{5.4}$$

$$z_1 = z + c \cdot t \tag{5.5}$$

   And the spherical surface equation is.

$$R^2 = (x_1 - x_o)^2 + (y_1 - y_o)^2 + (z_1 - z_o)^2. \tag{5.6}$$

where R is the radius of the mirror, we have chosen (x_o, y_o, z_o) the center of the mirror to be the origin (0,0,0).

$$R^2 = (x_1)^2 + (y_1)^2 + (z_1)^2. \tag{5.7}$$

$$R^2 = (x + a \cdot t)^2 + (y + b \cdot t)^2 + (z + c \cdot t)^2. \tag{5.8}$$

Solving for t we get (x_1, y_1, z_1).

2. Second, Calculate the vector normal to the spherical surface $\overrightarrow{R} = x_1\hat{i} + y_1\hat{j} + z_1\hat{k}$, it follows that.

$$\overrightarrow{U_b} = \overrightarrow{U_i} - 2 < \overrightarrow{U_i} \cdot \hat{R} > \hat{R}. \tag{5.9}$$

where $\overrightarrow{U_b}$ is the direction of the reflected beam, $\overrightarrow{U_i}$ is that of the incident beam, and $\hat{R}$ is the unit vector $\overrightarrow{R}/||\overrightarrow{R}||$.

To prove that the previous statement is true we must get

$$||\overrightarrow{U_b}||^2 = ||\overrightarrow{U_i}||^2$$

And since

$$(\overrightarrow{U_b})^2 = (\overrightarrow{U_i} - 2 < \overrightarrow{U_i} \cdot \hat{R} > \hat{R})^2.$$

$$||\overrightarrow{U_b}||^2 = ||\overrightarrow{U_i}||^2 - 4 < \overrightarrow{U_i} \cdot \hat{R} >^2 + 4 < \overrightarrow{U_i} \cdot \hat{R} >^2 .$$

$$||\overrightarrow{U_b}||^2 = ||\overrightarrow{U_i}||^2.$$

3. Third, we compute the point at which the reflected beam hits the focal surface.

4. Looping over the previous process, we obtain the shape/size of the reflected image, which is known as “the spot”.

The spot can be seen in figures (5.6) and (5.7), with the images radial distribution seen in figures (5.2) and (5.4) for 0° and 10° angle of incidence of the rays.

5.5.1 Corrector plate

The simulation here is the same as the one above but we need to ray-trace the refraction through the lens that is placed at the center of the primary mirror (the entrance).

For the refraction we use:

$$\hat{c} \cdot \hat{n} = -cos(\theta_i) \tag{5.10}$$

$$\hat{r} \cdot \hat{n} = -cos(\theta_r) \tag{5.11}$$

where $\hat{c}$ is the unit vector parallel to the incident beam, $\hat{n}$ is the unit vector parallel to the normal to the lens surface, $\hat{r}$ is the unit vector parallel to the refracted beam, θ_i is the incident angle, and θ_r is the refracted angle which is calculated with Snells law.

$$n_1 sin(\theta_i) = n_2 sin(\theta_r) \tag{5.12}$$

We know that since $\hat{c}, \hat{n}, \hat{r}$ are co-planar we can express r as.

$$\hat{r} = a\hat{c} + b\hat{n} \tag{5.13}$$

knowing that,

$$\hat{r} \cdot \hat{r} = 1 = a\hat{c} \cdot \hat{r} + b\hat{n} \cdot \hat{r} \tag{5.14}$$

we get,

$$\hat{r} \cdot \hat{r} = acos(\theta_i - \theta_r) - bcos(\theta_r) \tag{5.15}$$

and knowing that,

$$\hat{r} \cdot \hat{n} = -cos(\theta r) = a\hat{c} \cdot \hat{n} + b\hat{n} \cdot \hat{n} \tag{5.16}$$

we get,

$$\hat{r} \cdot \hat{n} = -acos(\theta_i) + b \tag{5.17}$$

therefor Using equations 5.15 and 5.17 we are able to solve for a and b.

$$a = sin(\theta_r)/sin(\theta_i). \qquad b = sin(\theta_r - \theta_i)/sin(\theta_i). \tag{5.18}$$

Using this information we are able to express $\hat{r}$ in terms of the incident angle θ_i and the refracted angle θ_r.

$$\hat{r} = \frac{1}{sin(\theta_i)}(sin(\theta_r)\hat{c} + sin(\theta_r - \theta_i)\hat{n}). \tag{5.19}$$

The only quantity left to be determined is the surface normal $\hat{n}$. using equation (5.1), but we need to place it's aspherical surface facing the front side with the center of the mirror placed at the lens center.

$$T(r) = -\frac{(r^4 - Ar^2)}{32(n_2 - 1)f^3} - \frac{T(0)}{2} \tag{5.20}$$

$$f(r, \theta, x) = -T(r) - \frac{(r^4 - Ar^2)}{32(n_2 - 1)f^3} - \frac{T(0)}{2} \tag{5.21}$$

$$\hat{n} = \nabla f \tag{5.22}$$

the surface normal is.

$$\hat{n} = -\hat{i} - \frac{4\,(r^3 - 2Ar)}{32(n_2 - 1)f^3}(cos(\theta)\hat{j} + sin(\theta)\hat{k}). \tag{5.23}$$

And it follows that after calculating the lens surface normal we are able to calculate the trajectory of the reflected beam from the mirror to the focal plane, knowing this trajectory provides us with information about our image, for example where does the imaged beam interact with the focal plane and consequently the characteristic of the spot like it's radius, it's shape (5.6), the distribution of the imaged points along the longitudinal direction i.e. figure (5.4), and it's radial distribution i.e. figure (5.2).

Having these parameters in hand we get to know if the chosen parameters would lead to a dependable design, if the viewing angle of the camera can be obtained and if adding a corrector in the camera will achieve the desired spot size.

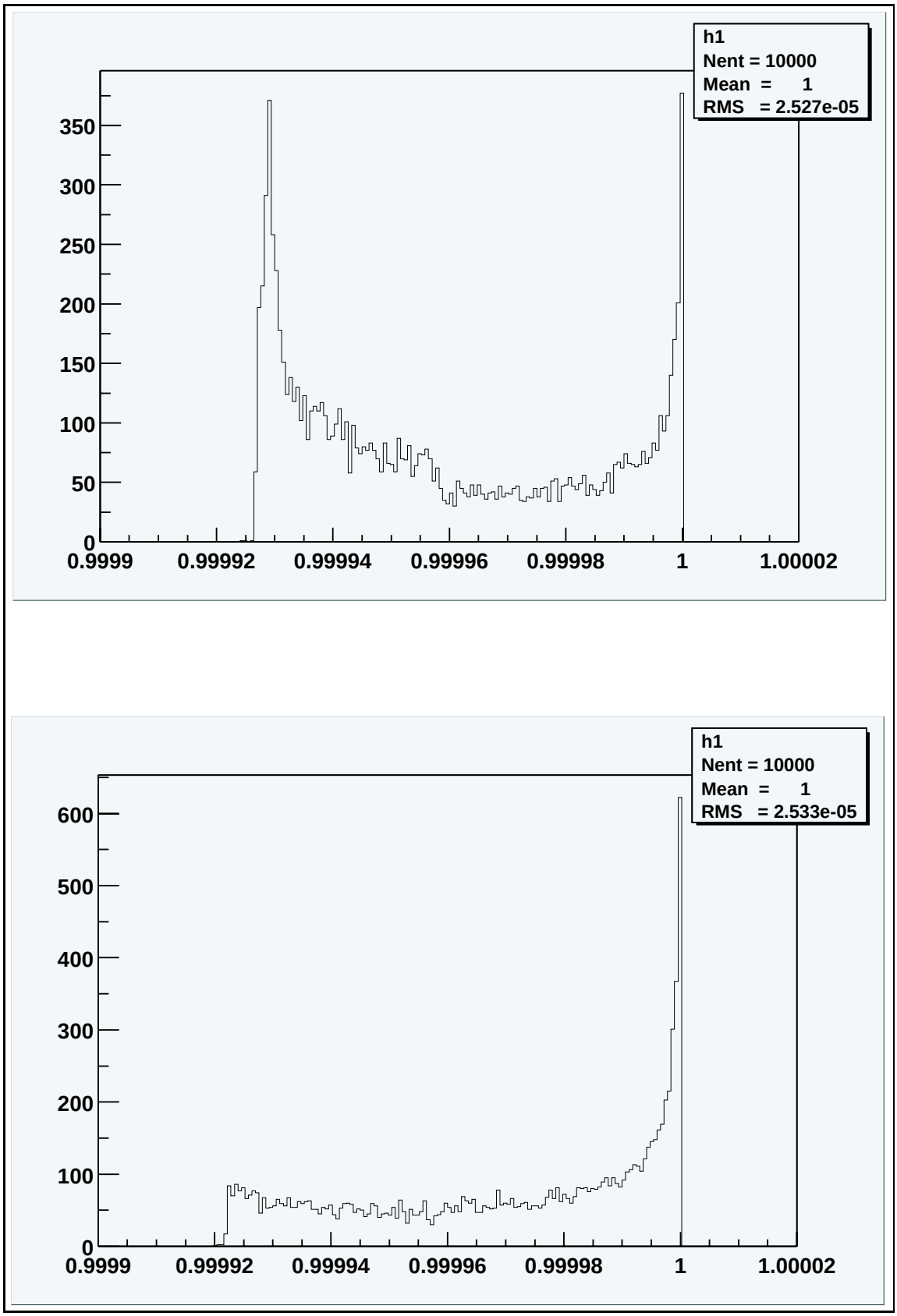

Figure 5.2. The radial distribution of the spot. From top to bottom the distribution without the corrector and with the corrector for 0° angle of incidence. Note that the distribution has been taken for the cosine of the radial angular position

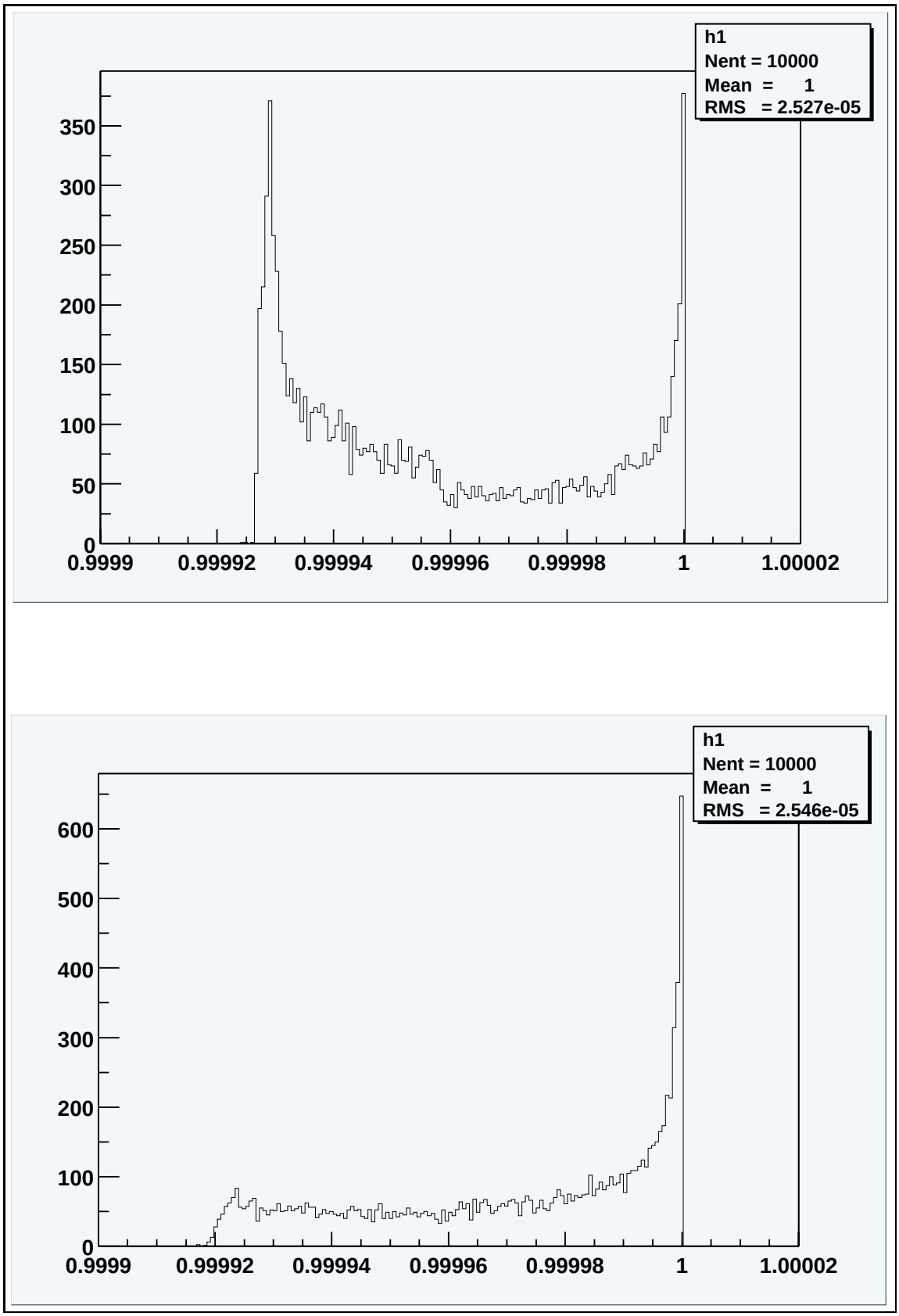

Figure 5.3. The radial distribution of the spot. From top to bottom the distribution without the corrector and with the corrector for 10° angle of incidence. Note that the distribution has been taken for the cosine of the radial angular position

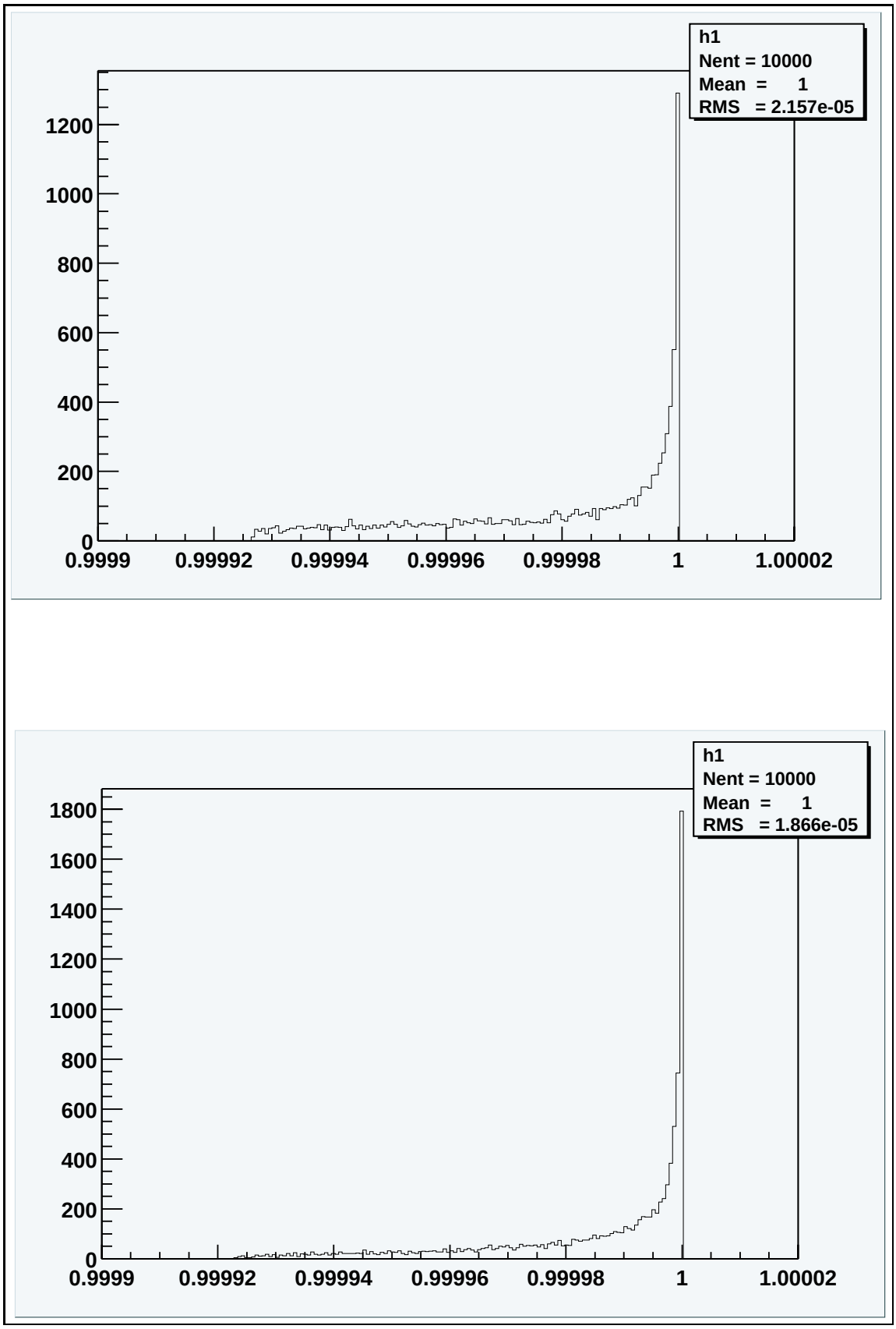

Figure 5.4. The longitudinal distribution of the spot. From top to bottom the distribution without the corrector and with the corrector for 0° angle of incidence. Note that the distribution has been taken for the cosine of the longitudinal angular position

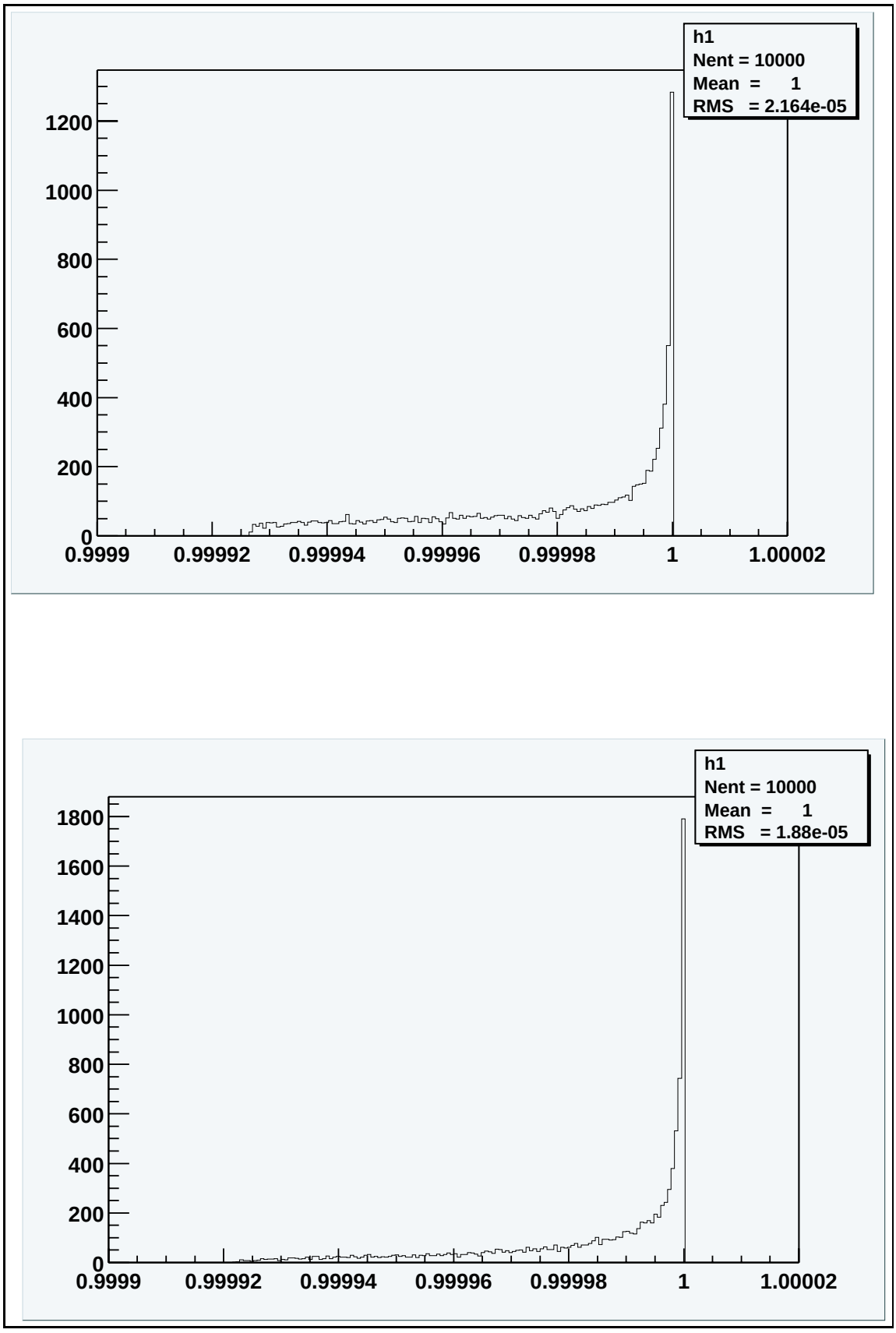

Figure 5.5. The longitudinal distribution of the spot. From top to bottom the distribution without the corrector and with the corrector for 10° degrees angle of incidence. Note that the distribution has been taken for the cosine of the longitudinal angular position

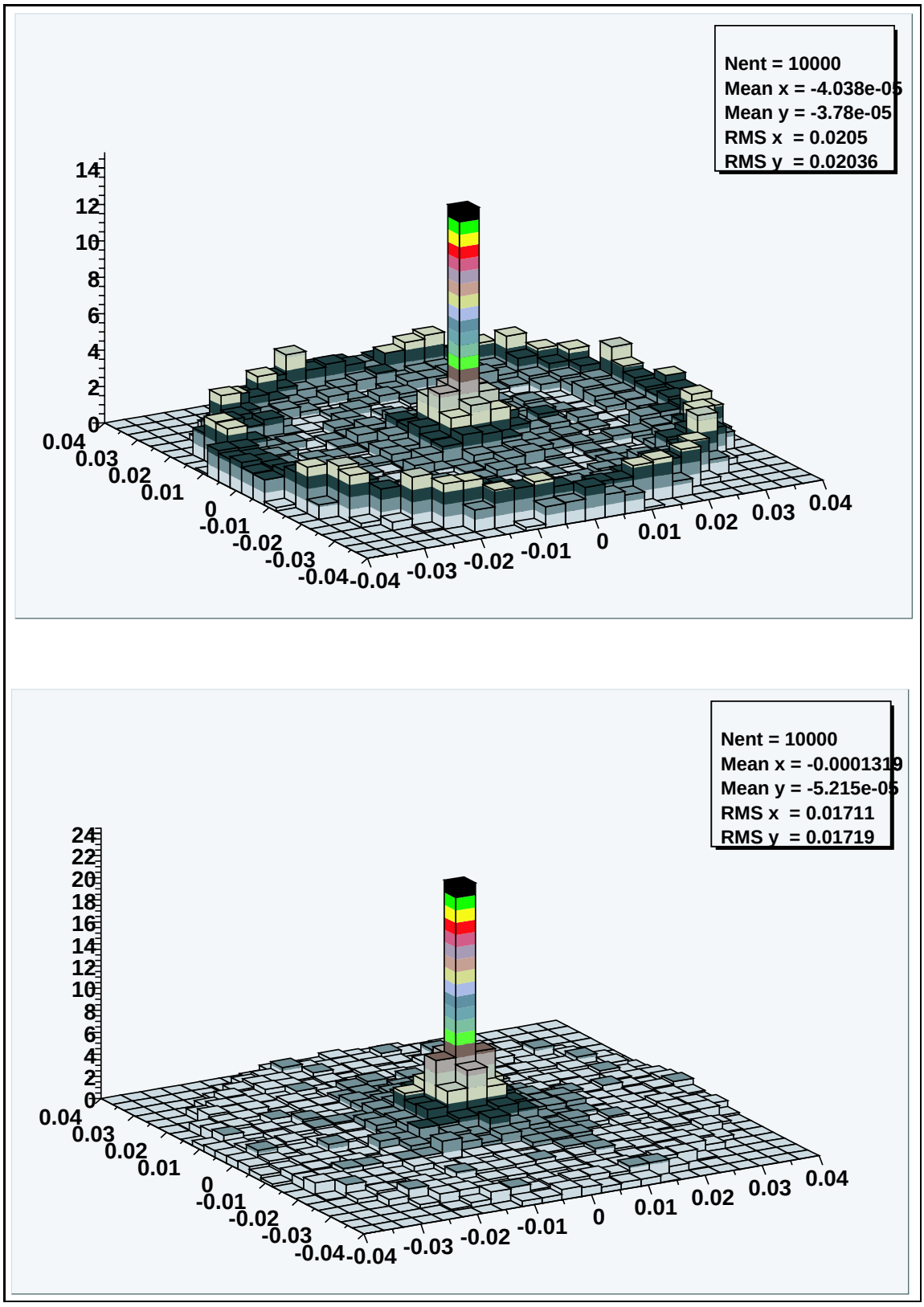

Figure 5.6. The spots 2-D histogram on the focal plane for 0°. From top to bottom the spots are without and with the corrector. Note how the spot is smaller when the corrector is used. The units used in the distribution is in (m)

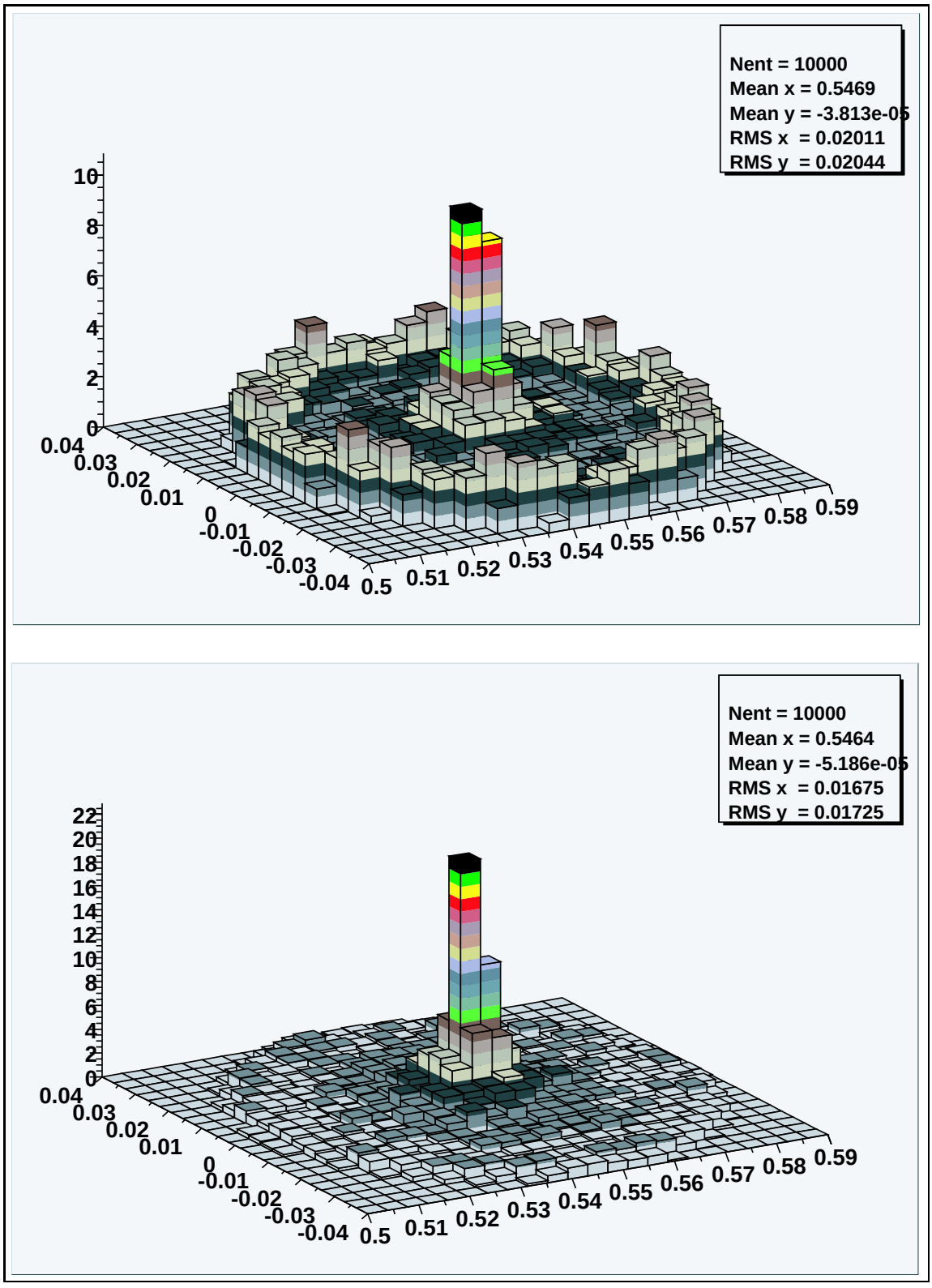

Figure 5.7. The spots 2-D histogram on the focal plane for 10°. From top to bottom the spots are without and with the corrector. Note how the spot is smaller when the corrector is used. The units used in the distribution is in (m)

Table 5.1. The RMS of the optical system with and without the corrector with an optimized focal length for the spherical focal plane surface.

RMS distribution		
$\theta°$	RMS without corrector plate ∘	RMS with corrector plate ∘
0°	0.3725°	0.2167°
5°	0.3728°	0.3147°
10°	0.3739°	0.3155°
15°	0.3757°	0.3169°
20°	0.3782°	0.3189°

CONCLUSION

The distribution figures (5.4) and (5.5) describes the distribution of the beams in the imaged spot along longitudinal direction for different angles, the root mean square of each distribution is calculated and then the location of the focal plane is optimized for the best achieved root mean square of the spot. Table (5.1) describes the root mean square RMS for distributions with and without the corrector, as it is the case for all angles the RMS for the spots is smaller with using the corrector.

The next distribution figures (5.2) and (5.3) are the radial distributions of the detected rays of the design with different incident angles of the rays i.e. 0° and 10°, for the detector design with the corrector and without it. The effective radius of the spot (the spot that contains 80 percent of the points lie within it) with the corrector added to the design is smaller than the one without the corrector, i.e. the radius of the spot is $0.033\ m$ with the corrector and $0.036\ m$ without the corrector.

As a conclusion adding the corrector to the optical design with such configuration would result in a smaller spot size and an improvement in the spot quality of the system.

REFERENCES

[1] M. Born and E. Wolf, *Principles of Optics* , (Pergamon Press, 1970) Chap. 6,p. 247-249.

[2] P. Sokolsky, *Introduction to Ultrahigh Energy Cosmic Ray Physics*, vol. 76 of Frontiers in physics. Pierre Sokolsky, Addison-Wesley Publishing company, 1989. Chap. 2, p.7

[3] T. Abu-Zayyad, *The Effect if Clouds on Air Showers Observation from Space*, 2002

[4] W.R.Leo, *Techniques for Nuclear and Particle Physics Experiments*, Springer-Verlag, Berlin, 1994

[5] T. Abu-Zayyad, Ph.D. thesis ,University of Utah, 2000

[6] K. Reil, Ph.D. thesis, University of Utah, 2002

[7] D.J. Bird, *et al.* Physical Review Letters 71, 3401 (1993).

[8] K. Greisen, Physical Review Letters 16, 748 (1966).

[9] G.T. Zatsepin and V.A. KuzminSov. Phys. JETP Lett. 4, 78 (1966).

[10] T. K. Gaisser, in *Comsic Rays and Particle Physics*, (Cambridge University Press, 1990),Chap. 15, p. 226.

[11] T. Gaisser and A.M. Hillas,*Proc.* 15^{th} ICRC, Plovdiv, Bulgaria, 8,353 (1977)

[12] G.Matthiae and P.Privitera,Auger Technical Note, GAP-98-039.

[13] R.Stao and J.A.Brllido C and H.C.Reis, Auger Technical Note, GAP-99-012.

[14] J.F.Krizmanic, *et al. Owl Roadmap to The Ultrahigh-Energy Universe.*Technical report, NASA, 2002.

[15] J.F.Krizmanic, J.F.Ormes, and R.E.Streitmatter, editors *Workshop on Observing Giant Cosmic Ray Air Showers From* $> 10^{20}$ *eV Particles From Space, AIP conference proceedings, AIP conference proceedings* 422, 1998.

[16] C.R.Wilkinson *et al. Geometrical Reconstruction with the High Resolution Fly's Eye Prototype Cosmic Ray Detector.* Astroparticle Physics, 12 (3):121-134, 1999.

[17] J.F.Krizmanic *et al. Simulated Performance of the Orbiting Wide-Angle Light-Collector* . 27^{th}-Int. Cosmic Ray Conference, Hamburg, 2001, 861